

# Electrocatalytic Reduction of CO<sub>2</sub> to Ethylene by Molecular Cu-Complex Immobilized on Graphitized Mesoporous Carbon

Mani Balamurugan, Hui-Yun Jeong, Venkata Surya Kumar Choutipalli, Jung Sug Hong, Hongmin Seo, Natarajan Saravanan, Jun Ho Jang, Kang-Gyu Lee, Yoon Ho Lee, Sang Won Im, Venkatesan Subramanian, Sun Hee Kim, and Ki Tae Nam\*

The electrochemical reduction of carbon dioxide (CO<sub>2</sub>) to hydrocarbons is a challenging task because of the issues in controlling the efficiency and selectivity of the products. Among the various transition metals, copper has attracted attention as it yields more reduced and C<sub>2</sub> products even while using mononuclear copper center as catalysts. In addition, it is found that reversible formation of copper nanoparticle acts as the real catalytically active site for the conversion of CO<sub>2</sub> to reduced products. Here, it is demonstrated that the dinuclear molecular copper complex immobilized over graphitized mesoporous carbon can act as catalysts for the conversion of CO<sub>2</sub> to hydrocarbons (methane and ethylene) up to 60%. Interestingly, high selectivity toward C<sub>2</sub> product (40% faradaic efficiency) is achieved by a molecular complex based hybrid material from CO<sub>2</sub> in 0.1 M KCl. In addition, the role of local pH, porous structure, and carbon support in limiting the mass transport to achieve the highly reduced products is demonstrated. Although the spectroscopic analysis of the catalysts exhibits molecular nature of the complex after 2 h bulk electrolysis, morphological study reveals that the newly generated copper cluster is the real active site during the catalytic reactions.

However, electrochemical CO<sub>2</sub> reduction reaction (CO<sub>2</sub>RR) is kinetically sluggish, which always requires large overpotential and also usually generates multiple products.<sup>[5,8–10]</sup> Interestingly, plants and algae efficiently utilize the photosynthetic process to convert CO<sub>2</sub> and water to various organic compounds and several attempts have been made to mimic the CO<sub>2</sub> reduction process.<sup>[11,12]</sup> Various kinds of electrocatalysts such as homogeneous,<sup>[13–15]</sup> heterogeneous,<sup>[3,16,17]</sup> and single-atom catalysts are explored for the electrochemical CO<sub>2</sub> conversions.<sup>[18–22]</sup> Among the electrocatalytic materials studied so far, the metal complexes have attracted significant importance, because they possess well-defined structures that can be easily tuned in molecular level.<sup>[15,23–26]</sup> However, the key issues that remain with the molecular systems are stability and current density. Therefore, significant interest in the development of electrocatalytic materials

## 1. Introduction


Electrochemical conversion of CO<sub>2</sub> to chemicals and fuels using electricity generated from renewable energy sources could be the alternate for the development of carbon-neutral fuels.<sup>[1–7]</sup>

Dr. M. Balamurugan, Dr. H.-Y. Jeong, J. S. Hong, H. Seo, Dr. N. Saravanan, J. H. Jang, K.-G. Lee, Y. H. Lee, S. W. Im, Prof. K. T. Nam  
 Department of Materials Science and Engineering  
 Seoul National University  
 1 Gwanak-ro, Seoul 08826, Republic of Korea  
 E-mail: nkitae@snu.ac.kr

V. S. K. Choutipalli, Prof. V. Subramanian  
 Inorganic and Physical Chemistry Laboratory  
 CSIR-Central Leather Research Institute, Adyar, Chennai 600 020, India

V. S. K. Choutipalli, Prof. V. Subramanian  
 Academy of Scientific and Innovative Research (AcSIR)  
 CSIR-CLRI Campus, Chennai 600020, India

Dr. S. H. Kim  
 Western Seoul Center  
 Korea Basic Science Institute (KBSI)  
 150, Bukhayeon-ro, Seodaemun-gu, Seoul 120-140, Korea

 The ORCID identification number(s) for the author(s) of this article can be found under <https://doi.org/10.1002/smll.202000955>.

DOI: 10.1002/smll.202000955

by immobilizing over nanocarbon support has been established to enhance catalytic activity, stability, and selectivity for electrochemical CO<sub>2</sub> reduction.<sup>[27–29]</sup> Several molecular complexes based on various transition metals are used as catalysts for CO<sub>2</sub>RR and most of them produced CO selectively. Among them, bipyridine, cyclam, porphyrins, and phthalocyanine-based catalysts are well studied with different metals. For example, Re(bpy)(CO)<sub>3</sub>Cl (bpy = 2,2'-bipyridine),<sup>[30]</sup> Ru(bpy)(CO)<sub>2</sub>Cl<sub>2</sub>,<sup>[31,32]</sup> [Mn(bpy)(CO)<sub>3</sub>Br],<sup>[33]</sup> and Ir pincer complexes<sup>[34]</sup> produced CO with high selectivity. The first row transition metal complexes such as [Ni(cyclam)]<sup>2+</sup> (cyclam = 1,4,8,11-tetraazacyclotetradecane),<sup>[35–37]</sup> iron and cobalt porphyrins and phthalocyanines also exhibited high stability and selectivity for CO production.<sup>[23,38–41]</sup> Similarly, a few copper complexes also exhibited electrochemical CO<sub>2</sub> reduction activity.<sup>[42,43]</sup> However, most of the above-mentioned catalysts displayed the production of simple C<sub>1</sub> product predominantly, and hydrocarbon-producing molecular based catalysts are scarce.

In this context, among the various metal complexes reported so far Cu-based metal complexes displayed hydrocarbon production and C<sub>2</sub> products during the electroreduction of CO<sub>2</sub> similar to the heterogeneous catalysts (Figure 1).<sup>[25,29,44–46]</sup> First, Bouwman and coworkers identified a dinuclear copper complex coordinated with pyridine and sulfur-containing ligand can

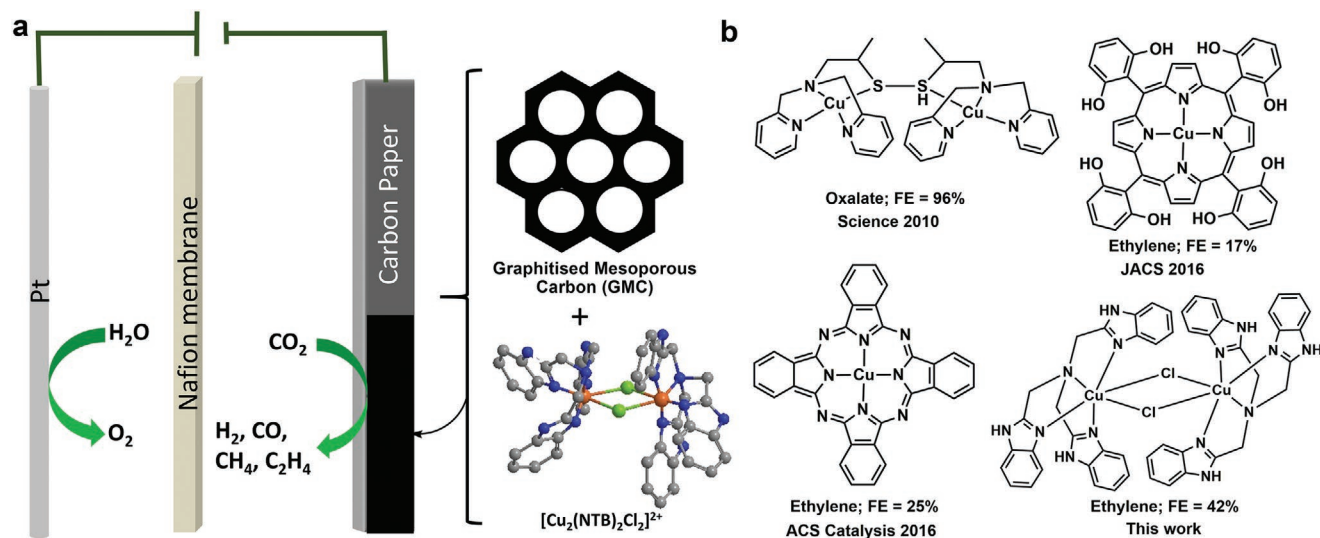


**Figure 1.** a) Cu complex employed as CO<sub>2</sub> reduction catalysts by immobilization on graphitized mesoporous carbon in CO<sub>2</sub> saturated 0.1 M KCl. b) The molecular complexes exhibiting C<sub>2</sub> product formation during electrocatalytic reduction of CO<sub>2</sub>.

electrochemically reduce CO<sub>2</sub> to oxalate. Based on the mechanistic and crystallographic study, formation of tetranuclear Cu cluster with two oxalate formed from the reaction of four Cu(I) sites with CO<sub>2</sub> was suggested as crucial reaction intermediate.<sup>[25]</sup> Recently, Wang group deposited the Cu-porphyrin complex over carbon nanoparticles and used as catalysts for the electrochemical CO<sub>2</sub> reduction to methane and ethylene with a faradaic efficiency (FE) of 25% and 17%, respectively.<sup>[29]</sup> Later, crystalline Cu(II) phthalocyanine (CuPc) immobilized on the carbon support was used as catalyst for CO<sub>2</sub> reduction and generated ethylene up to 25% FE. Based on X-ray photoelectron spectroscopy (XPS) analysis, it has been suggested that the molecular nature remains after bulk electrolysis in both porphyrin and phthalocyanine-based copper catalysts.<sup>[44]</sup> Very recently, restructuring of Cu complexes during electrocatalytic CO<sub>2</sub>RR has been revealed by in situ and operando X-ray absorption spectroscopy (XAS) characterization of various Cu systems such as CuPc, HKUST-1, and [Cu(cyclam)]Cl<sub>2</sub>. In particular, the reversible formation of ≈2 nm metallic Cu nanoclusters is identified as the active sites during the electrocatalytic reactions.<sup>[45]</sup> Similarly, the transient formation of metallic copper nanoparticle during the catalytic reduction of CO<sub>2</sub> was identified by XAS studies on the Cu–N–C material with single-site copper center. Although the postcatalytic analysis of the copper-based molecular systems reveals that the molecular nature remains unchanged after electrolysis, the in situ XAS analysis revealed the involvement of real active site under operating conditions. However, to enhance the selectivity issues and to understand more about the real active species responsible for the conversion of CO<sub>2</sub> to hydrocarbon, more molecular systems need to be studied.

In this study, we compared the activity of mononuclear Cu complex with dinuclear system with tris(2-benzimidazolylmethyl)amine (NTB) as common ligand, immobilized on graphitized mesoporous carbon for CO<sub>2</sub>RR. In 0.1 M KCl, the composite displayed higher selectivity for ethylene production along with methane and CO from CO<sub>2</sub> rather than

hydrogen evolution reaction (HER) (Figure 1). At –1.278 V versus reversible hydrogen electrode (RHE) the maximum FE (42%) was achieved for ethylene and total hydrocarbons (FE > 60%). Also, we identified that the C<sub>2</sub> product selectivity is dictated by other factors such as nuclearity of the complex system and nature of the carbon support and stirring of electrolyte. Based on the experimental observation, controlling the closeness of copper center, local pH, and limiting the mass transport during CO<sub>2</sub>RR essential to enhance the C<sub>2</sub> product selectivity was suggested. The XPS, electron paramagnetic resonance (EPR), and X-ray absorption near-edge structure (XANES) spectroscopic characterization revealed that the molecular nature of the complex system remains even after 2 h bulk electrolysis of the composite material. Moreover, the selectivity of the catalyst surpasses all the other molecular system for ethylene production, though the selectivity is lower than that of other heterogeneous copper materials.<sup>[47–52]</sup>

## 2. Results and Discussion

### 2.1. Synthesis and Characterization

The carbon-complex composite has been prepared by mixing the copper complexes with graphitized mesoporous carbon (GMC) followed by stirring for 6 h. The strong interaction between the copper complexes and GMC was observed due to the π–π stacking of the ligand with carbon support, which is confirmed by the decrease in absorption intensity in the UV–vis spectroscopy (Figure S1, Supporting Information) of the complex solution with and without GMC. The intensity of the d–d band of dimer [Cu<sub>2</sub>(NTB)<sub>2</sub>Cl<sub>2</sub>]<sup>2+</sup> at 340 nm was decreased when GMC was added suggesting the adsorption of the complex onto the surface of the GMC. Also, it has been previously reported that the NTB ligand can strongly interact with graphene oxide sheets.<sup>[19]</sup>

The excess or unabsorbed complex was removed by washing with methanol followed by water, and the composite GMC-[Cu<sub>2</sub>(NTB)<sub>2</sub>] was lyophilized and used as catalyst material. The similar procedure was used to prepare the GMC-[Cu(NTB)] using monomeric complex [Cu(NTB)NO<sub>3</sub>]<sup>+</sup> with GMC in methanol. The structure and activity of the composite GMC-[Cu<sub>2</sub>(NTB)<sub>2</sub>] were investigated by various characterization methods and discussed next.

### 2.1.1. Density Functional Theory (DFT) Calculations

To understand the interaction of the monomer versus dimer with the GMC, DFT calculation has been performed. From the DFT results, it is clear that the dimer (interaction energy -3.11 eV) has strong affinity with the carbon surface compared to the monomer (-0.70 eV) (Figures S2 and S3, Supporting Information). Moreover, structural reorganization of the dimer during the immobilization on the carbon surface has been observed due to the strong electrostatic interaction of the complex dimer with the GMC. The higher interaction energy may be resulting from the large size of the dimer and availability of high surface area to interact with graphene. From the calculated geometries of the dimeric copper complex with graphene (the Cu···Cu distance = 3.77 Å), interestingly, the two copper individual monomers were slightly moved apart leading to the formation of two monomers at short distance (the Cu···Cu distance = 4.49 Å). This may be due to the strong interaction of the copper dimer with graphene and weak bridging ability of the coordinated chlorines. The charge density analysis reveals that no significant variation of the charge on Cu atom in monomer is observed before and after the interaction with carbon sheet (Table S1, Supporting Information). Whereas, in case of dimer, one of the Cu atoms gains electrons from the graphene sheet. This observation is well supported by the frontier molecular orbital (FMO) analysis (Figures S3 and S4, Supporting Information), where highest occupied molecular orbital (HOMO) of the graphene-[Cu<sub>2</sub>(NTB)<sub>2</sub>Cl<sub>2</sub>] hybrid is predominantly located on graphene sheet and the lowest unoccupied molecular orbital (LUMO) is resided on one of the Cu-NTB fragments, which indicates the charge transfer from graphene sheet to Cu-NTB fragments of the dimer. On the other hand, in the case of graphene-[Cu(NTB)] hybrid, both HOMO and LUMO are located on the graphene sheet indicating the absence of charge transfer. The variation in charge on Cu (oxidation state) atoms in all the complexes is given in Table S1 (Supporting Information) and the FMO contours of the same are depicted in Figure S3 (Supporting Information). The difference in charge density on the copper atoms of the hybrid from the dimeric copper complex may play some key role during the catalytic reactions because it has been previously reported that mixed oxidation state of the catalytic center can boost the C-C coupling.<sup>[48]</sup>

## 2.2. Electrochemical CO<sub>2</sub> Reduction Activity

The electrochemical CO<sub>2</sub> reduction activity of the mono- and dimeric copper complexes was evaluated by cyclic voltammetry (CV) (Figure 2). Although the complexes show little activity, it

has been enhanced after immobilization of the complex over GMC. Initially, the redox behavior of the GMC-[Cu(NTB)] has been performed using CV measurements in 0.1 M aqueous KHCO<sub>3</sub> solution saturated with argon or CO<sub>2</sub>. In argon atmosphere the catalytic current for the hydrogen production started to evolve around -1.0 V versus RHE. After saturated with CO<sub>2</sub>, the current observed was negatively shifted due to the change in pH and reduction of CO<sub>2</sub>. Only one reduction peak was observed for the Cu(II) to Cu(I) redox in the CV, whereas during the oxidation more than two oxidation peaks was observed resulting from the metallic copper dissolution peak, which is generated due to the highly applied negative potential. Also, bulk electrolysis (BE) was conducted at various potential in the range from -1.27 to -1.57 V versus RHE (Figure S5, Supporting Information). Interestingly, at -1.37 V versus RHE, C<sub>2</sub>H<sub>4</sub> production reached the maximum FE of 22% along with CH<sub>4</sub> and CO and H<sub>2</sub> were also generated as coproducts (Figure 2c). Also, the NMR analysis of the electrolyte does not show any liquid products. Previously, it has been reported that the crystalline nature of the copper complex enhanced the C<sub>2</sub> product selectivity.<sup>[44]</sup> Based on the C<sub>2</sub> selectivity of the mononuclear CuNTB and previous studies on copper molecular complex systems, we anticipated that instead of the mononuclear complex, copper dimer may enhance the ethylene production as a result of two nearby copper center for C-C coupling during the reduction reactions.

Further, CO<sub>2</sub> reduction activity of GMC-[Cu<sub>2</sub>(NTB)<sub>2</sub>] was investigated and similar to the GMC-[Cu(NTB)] composite, the GMC-[Cu<sub>2</sub>(NTB)<sub>2</sub>] composite also shows multiple peaks on the oxidation region of the complex system in the cyclic voltammetry (Figure 2b). This kind of multiple redox behavior may be attributed to the restructuring of the molecular system and dissolution of the metallic copper during applied potential. Interestingly, the bulk electrolysis at -1.278 V versus RHE leading to the formation of ethylene with 35% FE and 12% methane and the total hydrocarbon selectivity reached 47% (Figure 2d). Compared to the GMC-[Cu(NTB)], the GMC-[Cu<sub>2</sub>(NTB)<sub>2</sub>] shows enhanced C<sub>2</sub> product as well as hydrocarbon selectivity. Previously, it has been reported that the crystallinity of CuPc plays an important role in the formation C<sub>2</sub>H<sub>4</sub> with 25% FE, in which the nearness of copper center was suggested as the origin of catalytic activity.<sup>[44]</sup> Similarly, the GMC-[Cu<sub>2</sub>(NTB)<sub>2</sub>] composite displayed higher selectivity compared to the GMC-[Cu(NTB)]. The effect of electrolyte concentration was also studied by varying the concentration of KHCO<sub>3</sub> and observed that the C<sub>2</sub> product selectivity has been decreased upon increasing the concentration of the electrolyte. Whereas upon changing the electrolyte from 0.1 M KHCO<sub>3</sub> to 0.1 M KCl the ethylene selectivity has been enhanced from 35% to 42% and methane selectivity from 12% to 18% and overall hydrocarbon selectivity reached over 60%.

To evaluate the importance of the carbon support, the dimer is immobilized on multiwalled carbon nanotube (MWCNT) and graphene oxide (GO) and studied the catalytic ability of the composites toward CO<sub>2</sub>RR (Figures S6 and S7, Supporting Information). Both MWCNT-[Cu<sub>2</sub>(NTB)<sub>2</sub>] and GO-[Cu<sub>2</sub>(NTB)<sub>2</sub>] exhibited lower C<sub>2</sub> product selectivity and higher methane production compared to GMC-[Cu<sub>2</sub>(NTB)<sub>2</sub>] (Figure 3a). Moreover, the CO<sub>2</sub> reduction product selectivity is also decreased

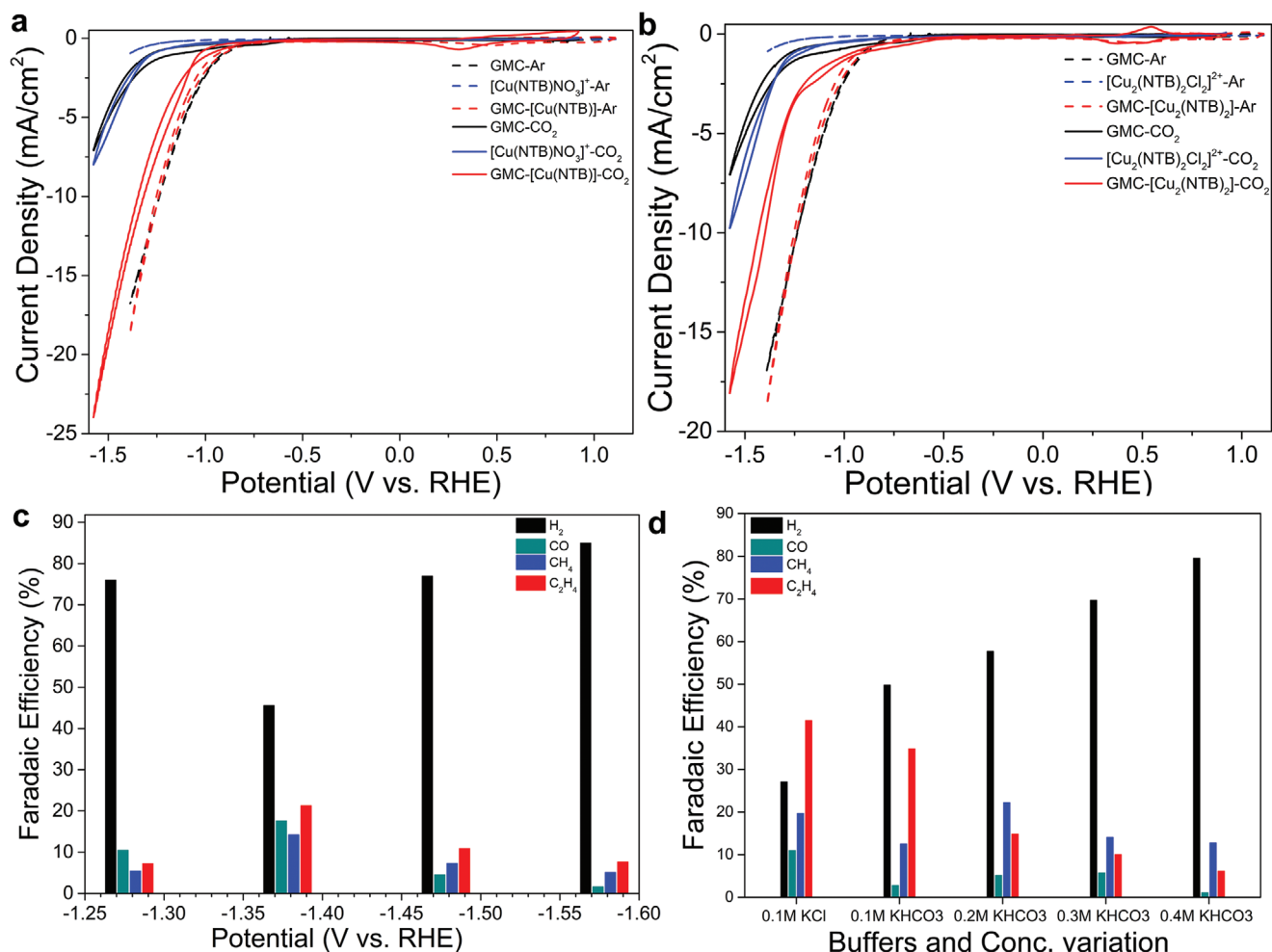


**Figure 2.** a) Cyclic voltammogram of GMC, [Cu(NTB)NO<sub>3</sub>]<sup>+</sup>, and GMC-[Cu(NTB)] measured in 0.1 M KCl under N<sub>2</sub> (black line) and CO<sub>2</sub> (red line) atmosphere at a scan rate of 10 mV s<sup>-1</sup>. b) Cyclic voltammogram of GMC, [Cu<sub>2</sub>(NTB)<sub>2</sub>Cl<sub>2</sub>]<sup>2+</sup>, and GMC-[Cu<sub>2</sub>(NTB)<sub>2</sub>] composites. c) Faradaic efficiencies of CO<sub>2</sub> reduction products catalyzed by GMC-[Cu(NTB)] at various applied electrode potentials. d) Faradaic efficiencies of CO<sub>2</sub> reduction products catalyzed by GMC-[Cu<sub>2</sub>(NTB)<sub>2</sub>] at different electrolytes and concentrations at -1.278 V versus RHE.

and favored HER. These results clearly indicate the importance of porous structure of the support material for the C–C coupling during the CO<sub>2</sub>RR. We assumed that the local pH may be enhanced during the reduction process inside the pores, which might enhance the C–C coupling to produce more C<sub>2</sub> product compared to the more flat surface carbon materials such as MWCNT and GO. This kind of porous effect on the C<sub>2</sub> selectivity has been already verified using nanoporous copper material and found that the flow field and local pH are the responsible factors for the C<sub>2</sub> product selectivity.<sup>[53]</sup> Moreover, theoretical calculation is also suggesting that at high pH, the CO–CO coupling pathway can be enhanced to produce ethylene.<sup>[54]</sup> To verify the local pH effect during the CO<sub>2</sub>RR catalyzed by the GMC-[Cu<sub>2</sub>(NTB)<sub>2</sub>], the effect of stirring of the electrolyte on the C<sub>2</sub> product selectivity has been studied (Figure 3b). Interestingly, gradual increase of the rotation speed from 100 to 300 rotation per minute (RPM) leads to decreased product selectivity of both ethylene and methane and enhances the CO release and HER. We assumed that controlling the mass transport inside the pores by stirring

can enhance the further reduction of CO to methane as well as coupling of CO to produce C<sub>2</sub> products. Also, possibly the local pH may be tuned by stirring, which affects the C<sub>2</sub> product selectivity. So, the porous nature of the carbon support also plays a critical role in enhancing the C<sub>2</sub> product selectivity by limiting the mass transport and by changing the local pH.

The potential dependent analysis was conducted in the range of -1.025 to 1.575 V versus RHE to find out the peak potential for ethylene FE (Figure 3c,d). Among the various applied potential at -1.27 V versus RHE, the highest ethylene production was observed and upon increasing the potential over -1.27 V, initially the methane production is slightly enhanced and ethylene production is decreased. Upon further increase of applied potential, the hydrogen evolution is also increased gradually and reached around 60% at -1.575 V versus RHE. The durability of the catalysts was monitored for 2 h and found that the FE of ethylene production is maintained for 2 h (Figure S8, Supporting Information). Also, the overall current density is increased gradually and reached the maximum total current

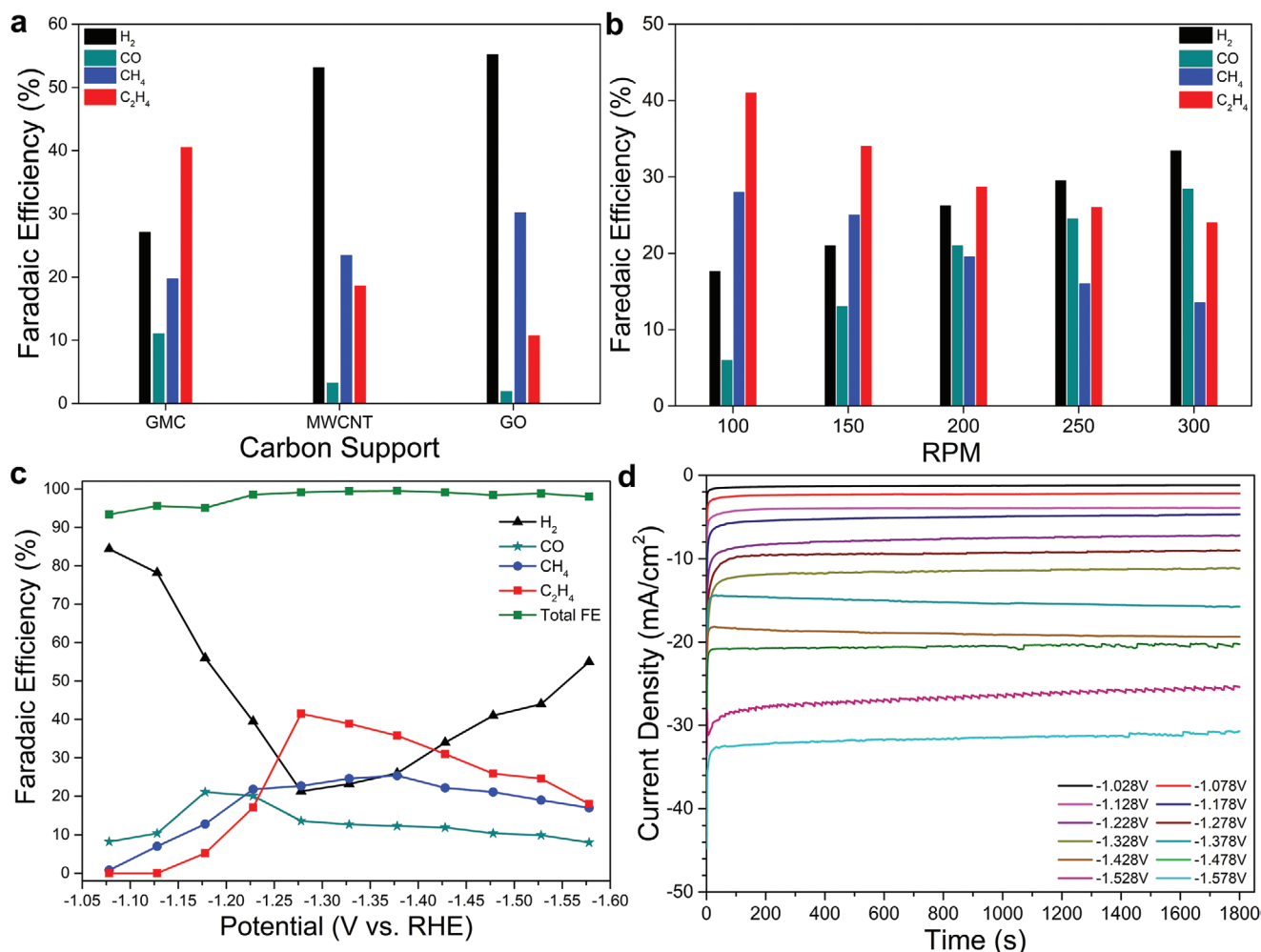


**Figure 3.** a) Effect of carbon support on product selectivity catalyzed by GMC-[Cu<sub>2</sub>(NTB)<sub>2</sub>] at -1.278 V versus RHE. b) Effect of stirring on product selectivity catalyzed by GMC-[Cu<sub>2</sub>(NTB)<sub>2</sub>] at -1.278 V versus RHE. c) Faradaic efficiencies of CO<sub>2</sub> reduction products catalyzed by GMC-[Cu<sub>2</sub>(NTB)<sub>2</sub>] at various applied electrode potentials. d) CO<sub>2</sub> reduction current density plot at various applied potentials catalyzed by GMC-[Cu<sub>2</sub>(NTB)<sub>2</sub>].

density of  $\approx 13 \text{ mA cm}^{-2}$  at -1.278 V versus RHE with 40% ethylene selectivity.

### 2.3. Spectroscopic Characterization

Due to the high applied negative potential, local structure modification is possible during the catalytic reaction. To investigate the chemical nature of the samples [Cu<sub>2</sub>(NTB)<sub>2</sub>Cl<sub>2</sub>]<sup>2+</sup>, GMC-[Cu<sub>2</sub>(NTB)<sub>2</sub>], and GMC-[Cu<sub>2</sub>(NTB)<sub>2</sub>]-BE, XPS has been performed and the Cu 2p XPS spectra of all the materials are shown in Figure 4a–c. The Cu 2p XPS spectra of [Cu<sub>2</sub>(NTB)<sub>2</sub>Cl<sub>2</sub>]<sup>2+</sup> exhibited 2p<sub>3/2</sub> and 2p<sub>1/2</sub> peaks at 934.3 and 954.2 eV, respectively, along with two strong satellite peaks at 942 and 962 eV corresponding to the +2 oxidation state of the copper center. The low energy peak is deconvoluted to both copper(II) and Cu(I) oxidation states and usually the dimeric copper complexes exhibit both Cu(II) and Cu(I) signals due to the reduction of some of the copper by intensity of the X-ray during the measurements. The Cu 2p XPS spectra of

GMC-[Cu<sub>2</sub>(NTB)<sub>2</sub>] show strong broad peaks at 934 and 953.6 eV along with satellite peaks of +2 oxidation state of the copper, which is strongly supporting the immobilization of the complex system over the GMC. After 2 h bulk electrolysis, the Cu 2p XPS spectra of GMC-[Cu<sub>2</sub>(NTB)<sub>2</sub>]-BE exhibited less intense peaks (934.3 eV and satellite peaks) corresponding to +2 oxidation state. Although, partially, the Cu(II) is reduced to Cu(I), the XPS signal clearly suggests the coexistence of both Cu(II) and Cu(I) after 2 h BE. Moreover, small peaks observed at 938 and 958 eV have been assigned to the multimeric copper system formed during the bulk electrolysis.

Further, the high-resolution N 1s spectrum of all those materials has been performed and the data are shown in Figure S9 (Supporting Information). The deconvoluted N 1s spectra of [Cu<sub>2</sub>(NTB)<sub>2</sub>Cl<sub>2</sub>]<sup>2+</sup> are fitted to three different nitrogens of NTB ligand. The peak at lowest binding energy of 399.0 eV is assigned to imine nitrogen of benzimidazolyl moiety coordinated with copper center and the peak at 400.3 eV is assigned to the uncoordinated amine nitrogen of the benzimidazolyl moiety. Also, another peak at 399.8 eV is deconvoluted and assigned to the tertiary nitrogen coordinated with copper

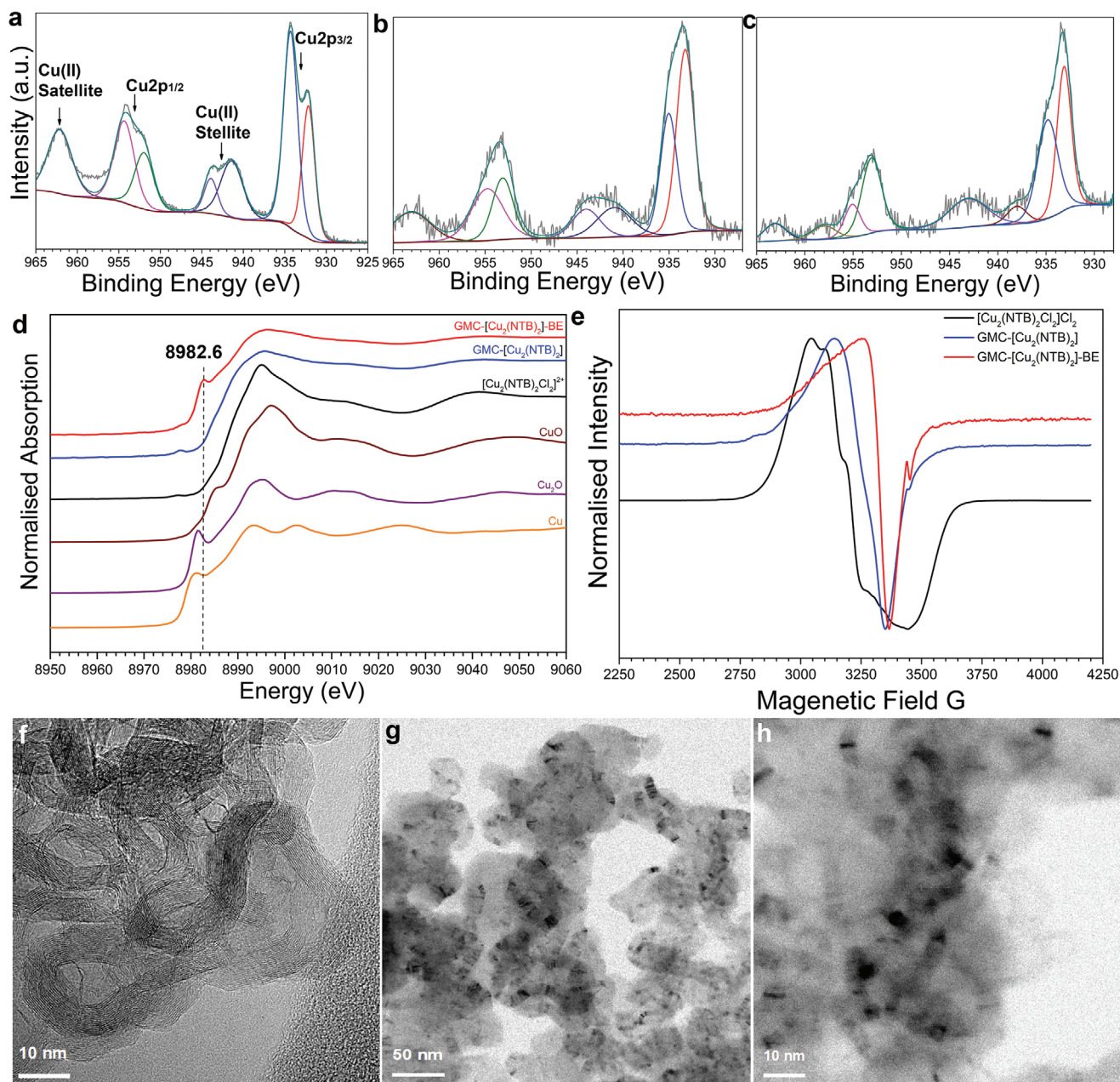


**Figure 4.** a) Cu-2p XPS spectrum of  $[\text{Cu}_2(\text{NTB})_2\text{Cl}_2]^{2+}$ . b) Cu-2p XPS spectrum of  $\text{GMC}[\text{Cu}_2(\text{NTB})_2]$ . c) Cu-2p XPS spectrum of  $\text{GMC}[\text{Cu}_2(\text{NTB})_2]\text{-BE}$ . d) Comparative XANES spectra of  $[\text{Cu}_2(\text{NTB})_2\text{Cl}_2]^{2+}$  and  $\text{GMC}[\text{Cu}_2(\text{NTB})_2]$  and  $\text{GMC}[\text{Cu}_2(\text{NTB})_2]\text{-BE}$  with Cu reference materials. e) EPR spectra of  $[\text{Cu}_2(\text{NTB})_2\text{Cl}_2]^{2+}$ ,  $\text{GMC}[\text{Cu}_2(\text{NTB})_2]$ , and  $\text{GMC}[\text{Cu}_2(\text{NTB})_2]\text{-BE}$ . f) Dark-field HR-TEM image of  $\text{GMC}[\text{Cu}_2(\text{NTB})_2]\text{-BE}$ . g, h) Bright-field HR-TEM image of  $\text{GMC}[\text{Cu}_2(\text{NTB})_2]\text{-BE}$ .

center. The similar N 1s spectra obtained for the before bulk electrolyzed sample  $\text{GMC}[\text{Cu}_2(\text{NTB})_2]$  suggest the immobilization of the complex over the GMC support. However, after 2 h bulk electrolysis, the sample  $\text{GMC}[\text{Cu}_2(\text{NTB})_2]\text{-BE}$  exhibited a different peak shape and the N 1s peak is deconvoluted in a similar way to the before bulk electrolyzed sample. In addition to both coordinated and uncoordinated nitrogens, another peak is deconvoluted for the uncoordinated imine nitrogen of the benzimidazolyl moiety as the intensity of the peak is slightly enhanced around 399 eV. We anticipated that structural

reorganization of the complex can happen at the applied negative potential and possibly the trigonal bipyramidal geometry cannot be retained and one of the benzimidazolyl moiety may be detached to attain the planarity and to bind strongly with the GMC surface. Overall, the XPS spectral results clearly suggest both the oxidation changes of the copper center as well as the structural reorganization of the complex system at negative applied potential.

To further investigate the changes in the oxidation state of the copper center after bulk electrolysis, XAS analyses were

conducted. The copper K-edge XANES spectrum of GMC-[Cu<sub>2</sub>(NTB)<sub>2</sub>]-BE along with original complex and after immobilization are shown in Figure 4d. The absorption edge energy of XANES can be very useful for determining the oxidation state and geometry of the metal center in the samples. Because higher X-ray energy is required to eject a core electron from a metal center with high charge, the higher oxidation state of the X-ray-absorbing metal can increase the absorption edge energy and linear relationships between the absorption edge energy and the oxidation state can be observed experimentally.<sup>[55,56]</sup> To understand the spectral pattern of the samples, the XAS of reference materials such as metallic Cu, Cu<sub>2</sub>O, and CuO have been performed and presented in Figure 4d. In the XANES spectrum of the [Cu<sub>2</sub>(NTB)<sub>2</sub>Cl<sub>2</sub>]<sup>2+</sup> and GMC-[Cu<sub>2</sub>(NTB)<sub>2</sub>], the absorption edge energy is located close to that of CuO, indicating that the valence state of copper in the dimer complex and GMC-[Cu<sub>2</sub>(NTB)<sub>2</sub>] is close to +2. The Cu K-edge XANES spectrum of [Cu<sub>2</sub>(NTB)<sub>2</sub>Cl<sub>2</sub>]<sup>2+</sup> and GMC-[Cu<sub>2</sub>(NTB)<sub>2</sub>] also shows very weak pre-edge peak at 8978 eV which corresponds to the characteristic 1s→3d transition. The bulk electrolyzed sample GMC-[Cu<sub>2</sub>(NTB)<sub>2</sub>]-BE also shows similar characteristic 1s→3d transition, which is assigned to the Cu(II) center. The copper K pre-edge is not observable for Cu(I) species because of the completely filled d<sup>10</sup> system. Whereas, the electric dipole allowed 1s to metal 4p orbital transition can be useful in predicting the geometry of the system. Previously, it has been observed that the energy and intensity of the signal depends on the ligand environment of the metal center.<sup>[57]</sup> So, the new rising edge observed at 8982.6 eV is assigned to the 1s→4p transition of the Cu(I) center with three coordinate geometries.<sup>[57–61]</sup> The rising edge observed at 8981 and 8981.5 eV, respectively, were also different from the XANES spectra of the metallic copper and Cu<sub>2</sub>O. The observed spectral behavior also suggests that because of the applied potential the immobilized complex undergoes structural reorganization. Similar to the XPS results, possibly one of the coordinated nitrogen atom may be detached from the coordination sphere to form more planar structure due to the strong π–π interaction of the ligand with GMC. Both XPS and XANES results clearly support the structural modification and change in oxidation state of the samples after bulk electrolysis.

EPR analysis has been performed to further investigate the change in the local structure of the metal center during electrolysis and the EPR spectra of [Cu<sub>2</sub>(NTB)<sub>2</sub>Cl<sub>2</sub>]<sup>2+</sup>, GMC-[Cu<sub>2</sub>(NTB)<sub>2</sub>], and GMC-[Cu<sub>2</sub>(NTB)<sub>2</sub>]-BE are shown in Figure 4e. The glass formed from the acetonitrile solution of the dinuclear [Cu<sub>2</sub>(NTB)<sub>2</sub>Cl<sub>2</sub>]<sup>2+</sup> complex exhibited the rhombic EPR signals with three g values at g = 2.261, 2.153, and 2.004 corresponding to the dimeric nature of the complex system. Previously, it has been reported that several chloride bridged dimeric copper complexes are exhibiting rhombic character and usually the hyperfine splitting is not well resolved.<sup>[62]</sup> After immobilization of the complex on GMC, the isotropic signal is observed indicating that the dimeric nature is modified during the immobilization of the complex over GMC. This result is in agreement with the theoretical calculation, which is also supported by the fact that each copper monomer is moved slightly apart over the GMC surface. The bulk electrolyzed sample GMC-[Cu<sub>2</sub>(NTB)<sub>2</sub>]-BE also exhibits isotropic broad signal at g<sub>⊥</sub> of

2.071 corresponding to Cu(II) center, due to the restructuring of the complex system after bulk electrolysis. Different from the GMC-[Cu<sub>2</sub>(NTB)<sub>2</sub>]-BE, the monomeric complex sample GMC-[Cu(NTB)]-BE exhibited tetragonal distortion and hyperfine splitting and the monomeric character is retained after bulk electrolysis (Figure S10, Supporting Information).

The XPS, XANES, and EPR spectral data suggest the structural reorganization and partial reduction of Cu(II) to Cu(I) after the bulk electrolysis of the immobilized complex. In addition, the molecular nature of the system is retained as the spectral behavior still remains even after 2 h bulk electrolysis. However, it may be due to the reversible restructuring of the catalytic systems and the real active site under operating conditions may be different from this observation. Also, previously it has been observed that reversible formation of the copper nanoparticle is the real active site under operating conditions.

So, we further conducted the morphological studies using high-resolution transmission electron microscopy (HR-TEM) and the results are shown in Figure 4f–h. The dark-field HR-TEM analysis of the sample GMC-[Cu<sub>2</sub>(NTB)<sub>2</sub>]-BE does not show any appreciable difference between the samples before and after bulk electrolysis (Figure S11, Supporting Information). However, the bright-field HRTEM analysis shows the formation of thin copper clusters during catalytic reactions. Although the spectral analysis of the bulk electrolyzed sample shows molecular nature, the morphological analysis shows the formation of copper cluster during catalytic reactions. So it is hypothesized that the copper cluster possibly stabilized by the ligands might be the real active site during the catalytic reduction of CO<sub>2</sub>.

### 3. Conclusion

In summary, we used the simple immobilization strategy to disperse the copper(II) complexes over graphitized mesoporous carbon and used as catalysts for CO<sub>2</sub>RR. Unlike metal complex as such, immobilization over GMC enhanced the catalytic activity for the electrochemical reduction of CO<sub>2</sub> to ethylene, methane, and CO with high C<sub>2</sub> product selectivity. Compared to previously reported copper molecular systems, the GMC-[Cu<sub>2</sub>(NTB)<sub>2</sub>] composite displayed high selectivity for ethylene (>40%) during electrolysis. The spectroscopic analyses such as XPS, EPR, and XANES suggest that the molecular nature of the system was not completely lost even after 2 h bulk electrolysis possibly due to restructuring. Compared to the composite with mononuclear copper center, the dimer composite exhibiting high selectivity for C<sub>2</sub> product may be due to the nearness of the copper center. Although the nuclearity of the system is not the general criteria for C<sub>2</sub>H<sub>4</sub> selectivity, it enhances the C–C bond-forming step in our composite system. Also, the morphological study clearly suggests the newly generated copper cluster might be the real active site under operating conditions. The importance of diatomic copper sites for C<sub>2</sub> product selectivity on the carbon support is under progress.

### 4. Experimental Section

**Materials:** Carbon mesoporous with average pore size of 6 and 13 nm, Nafion 117 solution (Sigma Aldrich), nitrotriacetic acid,

1,2-phenylenediamine, copper(II) nitrate trihydrate, and carbon paper (Toray) (Alfa Aesar) were purchased and used as received. Organic solvents such as methanol, ethanol, and acetonitrile (Daejung, Korea) were used without further purification. The ligand tris(2-benzimidazolylmethyl)amine (NTB) was synthesized as reported earlier.<sup>[63]</sup>

**Synthesis of Copper(II) Complexes:** Cu complexes  $[\text{Cu}(\text{NTB})\text{NO}_3]\text{NO}_3$  and  $[\text{Cu}_2(\text{NTB})_2\text{Cl}_2]\text{Cl}_2$  were prepared as reported previously.<sup>[64]</sup> Briefly,  $[\text{Cu}(\text{NTB})\text{NO}_3]\text{NO}_3$  was prepared by mixing copper(II) nitrate dissolved in ethanol with NTB in ethanol and stirred for 30 min. The greenish blue precipitate was filtered and washed with ethanol and then dried under vacuum.  $[\text{Cu}_2(\text{NTB})_2\text{Cl}_2]\text{Cl}_2$  was prepared from  $\text{CuCl}_2$  and NTB by mixing with a molar ratio of 1:1 in methanol/acetonitrile mixture and stirred for 1 h. Afterward, the complex was dissolved by adding more methanol and recrystallized by slow evaporation of the solvent. The resultant yellow crystals were filtered and washed with cold methanol and dried in air for 1 d.

**GMC-Cu Complex Composite Preparation:** First, the mesoporous carbon (4 mg) was dispersed in 1 mL of acetonitrile:ethanol mixture (90:10) by sonication for 5 min. Then (1.25 wt%) Nafion solution was introduced and the stirring was continued for another 5 min to completely disperse the carbon. Followed by (2 mg) copper(II) complexes were added in to the carbon-Nafion composite and shaken well for 6 h to attain the immobilization of the complex and equilibrium condition. Later, the composite was centrifuged and washed with methanol (1 mL) twice and centrifuged. The final composite material was freeze-dried to get dry powder.

**Computational Details:** All the geometry optimizations were carried out with DFT-based B3LYP hybrid functional in conjunction with 6-31G (d,p) Pople basis set.<sup>[65]</sup> The calculations were done with G16 suite of programme. Due to the complexity of the system, the vibrational analysis was not carried out for the complex systems. However, vibrational analysis was done for monomer and dimer forms of the substrate (Cu-NTB) to ensure that they are global minima on the potential energy surface.

**Electrochemical Measurements:** The electrochemical measurements were carried out using H-cell with a conventional three-electrode configuration. An Ag/AgCl electrode was used for the reference, and Pt wire was used as the counter electrode. The working and counter electrodes were separated by a Nafion 117 membrane. Carbon paper was used as the working electrode. Electrical contact to the carbon paper was made by fixing a copper wire at the edge of the carbon paper using silver paste, and the electrical contact was sealed with epoxy resin exposing a  $0.5 \times 0.5 \text{ cm}^2$  area of the carbon paper as the working area. To immobilize the catalyst on the carbon paper, the catalyst (4 mg) was dispersed in ethanol (1 mL) by sonication, and then, a sample of the as-prepared ink (60  $\mu\text{L}$ ) was drop-casted onto the carbon paper and dried with a heat gun, resulting in a catalyst loading of  $0.24 \text{ mg cm}^{-2}$ . Electrochemical measurements were conducted with a potentiostat (CHI600D, CH Instruments, USA). The electrolyte solutions were purged and saturated with Ar or  $\text{CO}_2$  for 30 min before measuring the CV or bulk electrolysis. During the CV measurements, the electrolyte was stirred to effectively supply dissolved  $\text{CO}_2$  to the electrode surface and detach the produced bubbles from the electrode. In addition, the electrode potentials measured with an Ag/AgCl reference electrode were converted to potentials versus the RHE.

To quantify the product amounts, a gas chromatograph equipped with a thermal conductivity detector (TCD) and a flame ionization detector (FID) (PerkinElmer, NARL8502 model 4003) was used. The gas products were separated with a Hayesep N and a Molesieve 13X column. Hydrogen, oxygen, and nitrogen were detected by TCD, and all other products were detected by FID. After the bulk electrolysis, 0.1 mL of gas was sampled from the headspace of the electrochemical cell and injected into the GC (Figure S12, Supporting Information). The number of moles was calculated from the area of the peaks and head space volume, and the area was calibrated using a standard gas (0.1 mol% of each gas species). All the FE values given in the manuscript are an average of three runs.

**Characterization:** The UV-visible spectra were measured using Agilent 8453 photodiode array spectrophotometer. The surface characteristics of the catalysts were examined by X-ray photoelectron spectroscopy (K-Alpha, Thermo Scientific Inc., UK). The XPS samples were prepared by embedding the catalyst powders in the surface of indium foils. The obtained XPS spectra were calibrated on the basis of the C1s peak by correcting the C—C peak position to 284.5 eV. The chemical structures of the metal sites in the catalysts were further investigated by X-ray absorption spectroscopy. XANES analyses were conducted using the BL10C beam line at the Pohang light source (PLS-II). The storage ring was operated with a ring current of 350 mA at 3.0 GeV operated in top-up mode. A monochromatic X-ray beam was obtained using a liquid-nitrogen-cooled Si double-crystal monochromator. XAS spectra were acquired in fluorescence mode under ambient conditions using a passivated implanted planar silicon (PIPS) detector. Energy calibration was carried out for each metal atom with reference metal foils. The obtained XANES spectra were analyzed with the ATHENA software packages following standard procedures.<sup>[66]</sup> EPR was performed using a Bruker EMX/Plus spectrometer equipped with a dual mode cavity (ER 4116DM). Low temperatures were achieved and controlled using a liquid He quartz cryostat (Oxford Instruments ESR900) with gas flow controller (Oxford Instruments ITC503). The experimental conditions are as follows: Microwave frequency 9.64 GHz (perpendicular mode), modulation amplitude 10G, modulation frequency 100 kHz, microwave power 0.94 mW (perpendicular mode), and temperature 5.7 K. Ten scans were added for each spectrum.

## Supporting Information

Supporting Information is available from the Wiley Online Library or from the author.

## Acknowledgements

This research was supported by Creative Materials Discovery Program through the National Research Foundation of Korea (NRF) funded by Ministry of Science and ICT (NRF-2017M3D1A1039377), the Global Frontier R&D Program of the Center for Multiscale Energy System funded by the National Research Foundation under the Ministry of Science and ICT, Korea (2012M3A6A7054855), the National Research Foundation of Korea (NRF) grant funded by the Korea government (MSIT) (NRF-2017R1A2B3012003), the KIST-SNU Joint Research Lab project (2V06170) under the KIST Institutional Program by the Korea government (Ministry of Science and ICT), BK21PLUS SNU Materials Division for Educating Creative Global Leaders (21A20131912052). K.T.N. appreciates the support from Institute of Engineering Research and Research Institute of Advanced Materials (RIAM) and Soft Foundry at Seoul National University.

## Conflict of Interest

The authors declare no conflict of interest.

## Keywords

$\text{CO}_2$  reduction, ethylene production, immobilization, mesoporous carbon, molecular copper complex

Received: February 15, 2020

Revised: April 17, 2020

Published online:



- [1] M. Halmann, *Nature* **1978**, 275, 115.
- [2] M. Aresta, A. Dibenedetto, A. Angelini, *Chem. Rev.* **2014**, 114, 1709.
- [3] J. L. Qiao, Y. Y. Liu, F. Hong, J. J. Zhang, *Chem. Soc. Rev.* **2014**, 43, 631.
- [4] C. W. Lee, N. H. Cho, S. W. Im, M. S. Jee, Y. J. Hwang, B. K. Min, K. T. Nam, *J. Mater. Chem. A* **2018**, 6, 14043.
- [5] K. D. Yang, C. W. Lee, K. Jin, S. W. Im, K. T. Nam, *J. Phys. Chem. Lett.* **2017**, 8, 538.
- [6] S. Nitopi, E. Bertheussen, S. B. Scott, X. Y. Liu, A. K. Engstfeld, S. Horch, B. Seger, I. E. L. Stephens, K. Chan, C. Hahn, J. K. Nørskov, T. F. Jaramillo, I. Chorkendorff, *Chem. Rev.* **2019**, 119, 7610.
- [7] W. J. Zhang, Y. Hu, L. B. Ma, G. Y. Zhu, Y. R. Wang, X. L. Xue, R. P. Chen, S. Y. Yang, Z. Jin, *Adv. Sci.* **2018**, 5, 1700275.
- [8] Q. Lu, F. Jiao, *Nano Energy* **2016**, 29, 439.
- [9] J. J. Wu, X. D. Zhou, *Chin. J. Catal.* **2016**, 37, 999.
- [10] S. J. Huo, Z. Weng, Z. S. Wu, Y. R. Zhong, Y. S. Wu, J. H. Fang, H. L. Wang, *ACS Appl. Mater. Interfaces* **2017**, 9, 28519.
- [11] J. Wang, Y. Guan, X. Yu, Y. Cao, J. Chen, Y. Wang, B. Hu, H. Jing, *iScience* **2020**, 23, 100768.
- [12] Y. Zhang, B. Han, Y. Xu, D. Zhao, Y. Jia, R. Nie, Z. Zhu, F. Chen, J. Wang, H. Jing, *ChemSusChem* **2017**, 10, 1742.
- [13] R. Francke, B. Schille, M. Roemelt, *Chem. Rev.* **2018**, 118, 4631.
- [14] N. Elgrishi, M. B. Chambers, X. Wang, M. Fontecave, *Chem. Soc. Rev.* **2017**, 46, 761.
- [15] H. Takeda, C. Cometto, O. Ishitani, M. Robert, *ACS Catal.* **2017**, 7, 70.
- [16] G. X. Zhao, X. B. Huang, X. X. Wang, X. K. Wang, *J. Mater. Chem. A* **2017**, 5, 21625.
- [17] H. Y. Kang, D. H. Nam, K. D. Yang, W. Joo, H. Kwak, H. H. Kim, S. H. Hong, K. T. Nam, Y. C. Joo, *ACS Nano* **2018**, 12, 8187.
- [18] H. Y. Jeong, M. Balamurugan, V. S. K. Choutipalli, E. S. Jeong, V. Subramanian, U. Sim, K. T. Nam, *J. Mater. Chem. A* **2019**, 7, 10651.
- [19] H. Y. Jeong, M. Balamurugan, V. S. K. Choutipalli, J. Jo, H. Baik, V. Subramanian, M. Kim, U. Sim, K. T. Nam, *Chem. - Eur. J.* **2018**, 24, 18444.
- [20] Y. Jiao, Y. Zheng, P. Chen, M. Jaroniec, S. Z. Qiao, *J. Am. Chem. Soc.* **2017**, 139, 18093.
- [21] D. Karapinar, A. Zitolo, T. N. Huan, S. Zanna, D. Taverna, L. H. G. Tizei, D. Giaume, P. Marcus, V. Mougél, M. Fontecave, *ChemSusChem* **2020**, 13, 173.
- [22] C. W. Lee, K. D. Yang, D. H. Nam, J. H. Jang, N. H. Cho, S. W. Im, K. T. Nam, *Adv. Mater.* **2018**, 30, e1704717.
- [23] C. Costentin, S. Drouet, M. Robert, J. M. Saveant, *Science* **2012**, 338, 90.
- [24] J. Schneider, H. F. Jia, K. Kober, D. E. Cabelli, J. T. Muckerman, E. Fujita, *Energy Environ. Sci.* **2012**, 5, 9502.
- [25] R. Angamuthu, P. Byers, M. Lutz, A. L. Speck, E. Bouwman, *Science* **2010**, 327, 313.
- [26] X. Zhang, Z. S. Wu, X. Zhang, L. W. Li, Y. Y. Li, H. M. Xu, X. X. Li, X. L. Yu, Z. S. Zhang, Y. Y. Liang, H. L. Wang, *Nat. Commun.* **2017**, 8, 14675.
- [27] J. Shen, R. Kortlever, R. Kas, Y. Y. Birdja, O. Diaz-Morales, Y. Kwon, I. Ledezma-Yanez, K. J. P. Schouten, G. Mul, M. T. M. Koper, *Nat. Commun.* **2015**, 6, 8177.
- [28] S. A. Yao, R. E. Ruther, L. H. Zhang, R. A. Franking, R. J. Hamers, J. F. Berry, *J. Am. Chem. Soc.* **2012**, 134, 15632.
- [29] Z. Weng, J. B. Jing, Y. S. Wu, Z. S. Wu, X. T. Guo, K. L. Materna, W. Liu, V. S. Batista, G. W. Brudvig, H. L. Wang, *J. Am. Chem. Soc.* **2016**, 138, 8076.
- [30] X. X. Qiao, Q. Q. Li, R. N. Schaugaard, B. W. Noffke, Y. J. Liu, D. P. Li, L. Liu, K. Raghavachari, L. S. Li, *J. Am. Chem. Soc.* **2017**, 139, 3934.
- [31] S. Oh, J. R. Gallagher, J. T. Miller, Y. Surendranath, *J. Am. Chem. Soc.* **2016**, 138, 1820.
- [32] C. W. Machan, M. D. Sampson, C. P. Kubiak, *J. Am. Chem. Soc.* **2015**, 137, 11540.
- [33] M. Bourrez, F. Molton, S. Chardon-Noblat, A. Deronzier, *Angew. Chem., Int. Ed.* **2011**, 50, 9903.
- [34] P. Kang, T. J. Meyer, M. Brookhart, *Chem. Sci.* **2013**, 4, 3497.
- [35] J. D. Froehlich, C. P. Kubiak, *J. Am. Chem. Soc.* **2015**, 137, 3565.
- [36] J. S. Song, E. L. Klein, F. Neese, S. F. Ye, *Inorg. Chem.* **2014**, 53, 7500.
- [37] J. D. Froehlich, C. P. Kubiak, *Inorg. Chem.* **2012**, 51, 3932.
- [38] C. Costentin, M. Robert, J. M. Saveant, A. Tatin, *Proc. Natl. Acad. Sci. USA* **2015**, 112, 6882.
- [39] C. Costentin, M. Robert, J. M. Saveant, *Acc. Chem. Res.* **2015**, 48, 2996.
- [40] T. Ogata, S. Yanagida, B. S. Brunschwig, E. Fujita, *J. Am. Chem. Soc.* **1995**, 117, 6708.
- [41] T. Atoguchi, A. Aramata, A. Kazusaka, M. Enyo, *J. Chem. Soc., Chem. Commun.* **1991**, 156.
- [42] R. J. Haines, R. E. Wittig, C. P. Kubiak, *Inorg. Chem.* **1994**, 33, 4723.
- [43] J. Wang, L. Y. Gan, Q. W. Zhang, V. Reddu, Y. C. Peng, Z. C. Liu, X. H. Xia, C. Wang, X. Wang, *Adv. Energy Mater.* **2019**, 9.
- [44] S. Kusama, T. Saito, H. Hashiba, A. Sakai, S. Yotsuhashi, *ACS Catal.* **2017**, 7, 8382.
- [45] Z. Weng, Y. S. Wu, M. Y. Wang, J. B. Jiang, K. Yang, S. J. Huo, X. F. Wang, Q. Ma, G. W. Brudvig, V. S. Batista, Y. Y. Liang, Z. X. Feng, H. L. Wang, *Nat. Commun.* **2018**, 9, 415.
- [46] D. Karapinar, N. T. Huan, N. R. Sahaie, J. Li, D. Wakerley, N. Touati, S. Zanna, D. Taverna, L. H. G. Tizei, A. Zitolo, F. Jaouen, V. Mougél, M. Fontecave, *Angew. Chem., Int. Ed.* **2019**, 58, 15098.
- [47] C. T. Dinh, T. Burdyny, M. G. Kibria, A. Seifitokaldani, C. M. Gabardo, F. P. G. de Arquer, A. Kiani, J. P. Edwards, P. De Luna, O. S. Bushuyev, C. Q. Zou, R. Quintero-Bermudez, Y. J. Pang, D. Sinton, E. H. Sargent, *Science* **2018**, 360, 783.
- [48] Y. S. Zhou, F. L. Che, M. Liu, C. Q. Zou, Z. Q. Liang, P. De Luna, H. F. Yuan, J. Li, Z. Q. Wang, H. P. Xie, H. M. Li, P. N. Chen, E. Bladt, R. Quintero-Bermudez, T. K. Sham, S. Bals, J. Hofkens, D. Sinton, G. Chen, E. H. Sargent, *Nat. Chem.* **2018**, 10, 974.
- [49] P. De Luna, R. Quintero-Bermudez, C. T. Dinh, M. B. Ross, O. S. Bushuyev, P. Todorovic, T. Regier, S. O. Kelley, P. D. Yang, E. H. Sargent, *Nat. Catal.* **2018**, 1, 103.
- [50] Y. J. Pang, J. Li, Z. Y. Wang, C. S. Tang, P. L. Hsieh, T. T. Zhuang, Z. Q. Liang, C. Q. Zou, X. Wang, P. De Luna, J. P. Edwards, Y. Xu, F. W. Li, C. T. Dinh, M. Zhong, Y. H. Lou, D. Wu, L. J. Chen, E. H. Sargent, D. Sinton, *Nat. Catal.* **2019**, 2, 251.
- [51] S. H. Zhong, X. L. Yang, Z. Cao, X. L. Dong, S. M. Kozlov, L. Falivene, J. K. Huang, X. F. Zhou, M. N. Hedhili, Z. P. Lai, K. W. Huang, Y. Han, L. Cavallo, L. J. Li, *Chem. Commun.* **2018**, 54, 11324.
- [52] H. Mistry, A. S. Varela, C. S. Bonifacio, I. Zegkinoglou, I. Sinev, Y. W. Choi, K. Kisslinger, E. A. Stach, J. C. Yang, P. Strasser, B. R. Cuenya, *Nat. Commun.* **2016**, 7, 12123.
- [53] K. D. Yang, W. R. Ko, J. H. Lee, S. J. Kim, H. Lee, M. H. Lee, K. T. Nam, *Angew. Chem., Int. Ed.* **2017**, 56, 796.
- [54] H. Xiao, T. Cheng, W. A. Goddard, R. Sundararaman, *J. Am. Chem. Soc.* **2016**, 138, 483.
- [55] J. Wong, F. W. Lytle, R. P. Messmer, D. H. Maylotte, *Phys. Rev. B* **1984**, 30, 5596.
- [56] I. Arcon, B. Mirtic, A. Kodre, *J. Am. Ceram. Soc.* **1998**, 81, 222.
- [57] M. L. Baker, M. W. Mara, J. J. Yan, K. O. Hodgson, B. Hedman, E. I. Solomon, *Coord. Chem. Rev.* **2017**, 345, 182.
- [58] J. M. Brown, L. Powers, B. Kincaid, J. A. Larrabee, T. G. Spiro, *J. Am. Chem. Soc.* **1980**, 102, 4210.

- [59] L. S. Kau, D. J. Spirasolomon, J. E. Pennerhahn, K. O. Hodgson, E. I. Solomon, *J. Am. Chem. Soc.* **1987**, *109*, 6433.
- [60] M. J. Pushie, E. Stefaniak, M. R. Sendzick, D. Sokaras, T. Kro, K. L. Haas, *Inorg. Chem.* **2019**, *58*, 15138.
- [61] C. H. Kjaergaard, M. F. Qayyum, S. D. Wong, F. Xu, G. R. Hemsworth, D. J. Walton, N. A. Young, G. J. Davies, P. H. Walton, K. S. Johansen, K. O. Hodgson, B. Hedman, E. I. Solomon, *Proc. Natl. Acad. Sci. USA* **2014**, *111*, 8797.
- [62] A. Klein, K. Butsch, S. Elmas, C. Biewer, D. Heift, S. Nitsche, I. Schlipf, H. Bertagnolli, *Polyhedron* **2012**, *31*, 649.
- [63] L. K. Thompson, B. S. Ramaswamy, E. A. Seymour, *Can. J. Chem.* **1977**, *55*, 878.
- [64] L. K. Thompson, B. S. Ramaswamy, R. D. Dawe, *Can. J. Chem.* **1978**, *56*, 1311.
- [65] K. Raghavachari, *Theor. Chem. Acc.* **2000**, *103*, 361.
- [66] B. Ravel, M. Newville, *J. Synchrotron Radiat.* **2005**, *12*, 537.